SKI Report 2004:34

Research

Sensitivity Study on Clad Tube Failure under Reactivity Initiated Accidents in Light Water Reactors

Lars Olof Jernkvist

August 2004

ISSN 1104–1374
ISRN SKI-R-04/33-SE

SKI

SKI Perspective

Background and purpose of the project

Over the last 10 years the behaviour of nuclear fuel during reactivity initiated accidents has been studied to investigate the failure threshold as a function of burnup. Experimental programmes performed in the CABRI test reactor (France) and in the Nuclear Safety Research Reactor (Japan) have indicated that cladding failure and fuel dispersion of high burnup fuel may occur at enthalpy values lower than previously estimated.

At the beginning of 1995 SKI issued fuel and cladding failure limits based on available test data. It was envisaged at that time that the failure limits should be re-evaluated when more information was available. Since then SKI has joined the OECD-IRSN CABRI water loop project at the end of 2000. The purpose was to gain information on the failure threshold for nuclear fuel cladding as a function of burnup, especially for modern cladding materials and during prototypical conditions.

In 2003 SKI initiated a study, in cooperation with the Swedish nuclear utilities, to recommend more relevant fuel failure limits for reactivity initiated accidents.

The work presented in this report is the third part of the study. In the report a sensitivity study is performed to quantify the influence of applied power pulse shape, power pulse width and clad-to-water heat transfer models on the calculated fuel rod failure thresholds for reactivity initiated accidents. In the first part a strain-based failure criterion was formulated based on mechanical tests and compared with experimental tests and other failure criterion. This is reported in SKI report 2004:32. In the second part of the study failure thresholds were calculated by use of best-estimate computational methods and reported in SKI report 2004:33.

Results

This project has contributed to the research goal of giving a basis for SKIs supervision by means of evaluating and modelling the nuclear fuel cladding failure threshold during a design base accident. The project has also contributed to the research goal to develop the competence about licensing of fuel at high burnup, which is an important safety issue.

Project information

Responsible for the project at SKI has been Jan in de Betou.
SKI Reference: 14.06-011070/02149

SKI Report 2004:34

Research

Sensitivity Study on Clad Tube Failure under Reactivity Initiated Accidents in Light Water Reactors

Lars Olof Jernkvist

Quantum Technologies AB
Uppsala Science Park
SE-751 83 Uppsala
Sweden

August 2004

List of contents

Summary

As a supplement to the best-estimate assessment of burnup-dependent fuel rod failure thresholds for reactivity initiated accidents (RIAs) by Jernkvist and Massih (2004), a parametric sensitivity study has been performed by use of the SCANAIR-3.2 computer program. The study was aimed to quantify the influence of applied power pulse shape, power pulse width and clad-to-water heat transfer models on the calculated fuel rod failure thresholds for RIA in pressurized- and boiling water reactors.

The parametric study was restricted to a specific fuel rod axial peak radial average burnup of 48 $MWd(kgU)^{-1}$. For this burnup, key fuel rod parameters were calculated for a spectrum of power pulse shapes and pulse widths, and also for various clad-to-water heat transfer models. The results indicate, that of the three factors investigated, only the pulse shape and pulse width influence the calculated fuel rod failure thresholds for RIA, which are here defined in terms of maximum allowable radial average fuel enthalpy.

The shape of the applied power pulse was found to have a significant impact on the calculated enthalpy threshold for fuel rod failure. The performed parametric study of pulse shapes was based on sixteen different power pulses, all of which were obtained from three-dimensional core analyses of postulated RIAs with zero or near-zero initial power in both pressurized- and boiling water reactors. A simple Gaussian pulse shape was also included in the parametric study, and it was found that the enthalpy thresholds calculated with the Gaussian power pulse were about 5% lower than those calculated with the most restricting of the pulse shapes obtained from three-dimensional core analyses. Hence, the use of a Gaussian power pulse in computer analyses of RIA leads to moderate conservatism in the calculated fuel rod failure thresholds.

Also the width of the applied power pulse was found to affect the calculated enthalpy threshold for fuel rod failure, in particular for power pulses narrower than about 50 ms. For the RIAs in pressurized- and boiling water reactors considered in our study, the enthalpy thresholds were found to drop by approximately 200 $J(gUO_2)^{-1}$ when reducing the pulse width from 50 to 5 ms.

The prediction of fuel rod failure was found to be practically unaffected by the models applied for clad-to-water critical heat flux and supercritical heat transfer. The explanation to this rather surprising result is that clad tube failure is predicted early during the RIA in our computer analyses. At this early stage of an RIA, the cladding temperature is governed primarily by the pellet-to-clad heat transfer and only to a lesser extent influenced by clad-to-water heat transfer.

Sammanfattning

I tillägg till fastställandet av utbränningsberoende bränsleskadegränser för reaktivitets-initierade olyckor (RIA) med hjälp av ”best-estimate” metodik (Jernkvist och Massih, 2004), har en parametrisk känslighetsanalys genomförts med beräkningsprogrammet SCANAIR-3.2. Syftet med känslighetsanalysen var att bestämma inverkan av ansatt pulsform, pulsvidd och modell för värmeöverföring från kapslingsrör till vatten, på de beräknade bränsleskadegränserna för RIA i tryck- och kokvattenreaktorer.

Känslighetsanalysen begränsades till en specifik utbränning om 48 $MWd(kgU)^{-1}$, vilken här avser maximal axiell nodutbränning i bränslestaven. Vid denna utbränning studerades bränslestavbeteendet genom att beräkna ett antal nyckelparametrar för olika val av pulsform, pulsvidd och värmeöverföringsmodeller. Resultaten visar att av de tre variabler som studerats, så har endast pulsform och pulsvidd någon nämnvärd inverkan på de beräknade bränsleskadegränserna för RIA. Dessa gränser definieras här i form av maximalt tillåtet radiellt medelvärde för bränsleentalpin under transienten.

Effektpulsens form visade sig ha en betydande inverkan på de beräknade bränsleskade-gränserna. Den genomförda känslighetsanalysen med avseende på pulsform baserades på 16 olika effektpulser för RIA i såväl tryck- som kokvattenreaktorer, vilka bestämts genom tredimensionell härdanalys av postulerade RIA med initialeffekt nära noll. Dessutom inkluderades en enkel Gaussformad effektpuls i studien, och det visade sig att entalpigränserna för bränsleskada beräknade med den Gaussformade pulsen var ungefär 5 % lägre än de gränser som erhölls med de mest begränsande av pulserna bestämda genom tredimensionell härdanalys. Således leder användandet av en Gaussformad effektpuls i datoranalyser av RIA till måttlig konservatism i beräknade bränsle-skadegränser.

Även effektpulsens vidd visade sig påverka de beräknade bränsleskadegränserna, i synnerhet för pulsvidder understigande 50 ms. De beräknade entalpigränserna för bränsleskada reducerades med ungefär 200 $J(gUO_2)^{-1}$, då pulsvidden minskades från 50 till 5 ms i våra analyser av RIA i tryck- och kokvattenreaktorer.

Predikteringen av bränsleskada var i de genomförda analyserna praktiskt taget opåverkad av vilka modeller som användes för kritiskt värmeflöde och superkritisk värmeöverföring från kapslingsrör till vatten. Förklaringen till detta något förvånande resultat är att kapslingsröret i våra analyser antas brista tidigt under RIA. Under denna tidiga fas av RIA bestäms kapslingstemperaturen främst av värmeöverföringen från bränslekuts till kapslingsrör, och påverkas endast till ringa del av värmeöverföringen från kapslingsrör till vatten.

1 Introduction

This report documents a parametric sensitivity study, which was performed as a supplement to the assessment of burnup-dependent fuel rod failure thresholds for reactivity initiated accidents reported by Jernkvist and Massih (2004). The purpose of the study was to quantify the influence of applied power pulse shape, power pulse width and clad-to-water heat transfer models on the calculated fuel rod failure thresholds. Key fuel rod parameters, most important of which is the threshold fuel enthalpy for failure, were calculated for a spectrum of power pulse shapes and pulse widths, and also for various clad-to-water heat transfer models. The calculations were made with the same computer codes and input data as used in determination of the burnup-dependent fuel rod failure thresholds (Jernkvist & Massih, 2004). However, the parametric study did not span the entire range of fuel burnup, but was restricted to a specific axial peak radial average burnup of 48 $MWd(kgU)^{-1}$.

The pulse shapes considered in the parametric study were those obtained from three-dimensional core analyses of reactivity initiated accidents with SIMULATE-3K, performed for the Ringhals 2 and 3 pressurized water reactors by Gabrielson (2004), and for the Oskarshamn 3 boiling water reactor by Wiksell (2003). Moreover, a simple analytical Gaussian power pulse was included in the parametric study for comparison.

The pulse widths considered in the study ranged from 5 to 100 ms. These numbers refer to the full width at half maximum (FWHM) of the pulses. In addition, a slow quasi-stationary pulse was included for comparison. The width of this pulse was 50 s.

The impact of clad-to-water heat transfer on the fuel rod failure behaviour was studied by applying alternative models for clad-to-water critical heat flux and for supercritical heat transfer under film boiling. More specifically, two models for critical heat flux and three models for heat transfer under film boiling were used in the parametric study.

The outline of the report is as follows:
Input and models applied in analyses are first documented in section 2. Results of the parametric study are then presented in sections 3 to 5, which deal with the influence of pulse shape, pulse width and clad-to-water heat transfer, respectively. Conclusions of the study are finally drawn in section 6, where the results are discussed in light of their relevance to the calculation of fuel rod failure thresholds for RIA.

2 Bases of performed analyses

The reactivity initiated accidents (RIAs) considered in this paper are the rod ejection accident (REA) in pressurized water reactors (PWRs) and the control rod drop accident (CRDA) in boiling water reactors (BWRs). Typical power pulse shapes for these events have been determined by use of the three-dimensional time-dependent neutronics code SIMULATE-3K, as reported by Vattenfall Bränsle and OKG, (Gabrielson, 2004) and (Wiksell, 2003). In the present report, the fuel rod thermo-mechanical behaviour under RIA was analysed by use of the SCANAIR-3.2 computer code (Federici et al., 2000). Since SCANAIR lacks models for simulation of long-term steady-state irradiation, the FRAPCON-3.2 fuel performance code was used to establish burnup-dependent initial conditions to the transient analyses (Berna et al., 1997).

The calculations were made with the same input and computational models as used in determination of the burnup-dependent fuel rod failure thresholds (Jernkvist & Massih, 2004). However, the parametric study did not span the entire range of fuel burnup, but was restricted to a specific axial peak radial average burnup of 48 $MWd(kgU)^{-1}$. The applied methodology and key input are summarized below.

2.1 Fuel rod design

The fuel considered in analyses of PWR REA is a 17×17 design (Gabrielson, 2004). In analyses of BWR CRDA, the considered fuel design is 10×10 (Wiksell, 2003). The key properties of these designs are summarized in table 2.1.

Design parameter		**PWR fuel rod 17×17**	**BWR fuel rod 10×10**
Fuel rod active length	[mm]	3658	3680
Fuel rod pitch	[mm]	12.6	13.0
Fuel rod fill gas		He	He
Fill gas pressure	[MPa]	2.50	0.60
Fuel pellet material		UO_2	UO_2
Fuel pellet density	[% of theoretical]	95.0	96.7
U-235 enrichment	[%]	3.80	4.00
Fuel pellet diameter	[mm]	8.165	8.480
Pellet dish volume fraction	[%]	1.40	1.12
Clad tube material		Zircaloy-4	Zircaloy-2
Clad outer diameter	[mm]	9.550	9.840
Clad wall thickness	[mm]	0.610	0.605

Table 2.1: Fuel rod designs considered in analyses.

2.2 Steady-state base irradiation

Steady-state base irradiation up to a burnup of approximately 42 MWd(kgU)$^{-1}$ (rod average) and 48 MWd(kgU)$^{-1}$ (radial average, axial peak) was simulated by use of FRAPCON-3.2. Core cooling conditions corresponding to nominal conditions in the Ringhals 3 PWR and the Oskarshamn 3 BWR were assumed in these simulations; see table 2.2.

Parameter		PWR Ringhals 3	BWR Oskarshamn 3
Nominal thermal power	[MW]	2775	3020
Average linear heat generation rate	[kWm^{-1}]	18.3	12.7
Coolant pressure	[MPa]	15.5	7.0
Coolant inlet temperature	[K]	557	550
Subchannel mass flow	[gs^{-1}]	327.5	174.6
Subchannel mass flux	[kg(m^{2}s)$^{-1}$]	3759	1878

Table 2.2: Core conditions applied in simulations of steady-state base irradiation.

The postulated steady-state power history and axial power distribution for the PWR fuel rod are shown in figures 2.1 and 2.2, whereas figures 2.3 and 2.4 show the postulated steady-state irradiation history and power distribution for the BWR rod. The axial power profiles were assumed not to change during the irradiation history.

The rods were discretized into ten equally long axial segments. This discretization was used in simulations of both the steady-state base irradiation and the reactivity initiated accident. The calculated clad oxide thickness and hydrogen content at end of base irradiation are shown in figures 2.5 and 2.6. These corrosion properties were calculated by use of best-estimate models for standard Zircaloy-2 and Zircaloy-4 cladding in FRAPCON-3.2 (Berna et al., 1997).

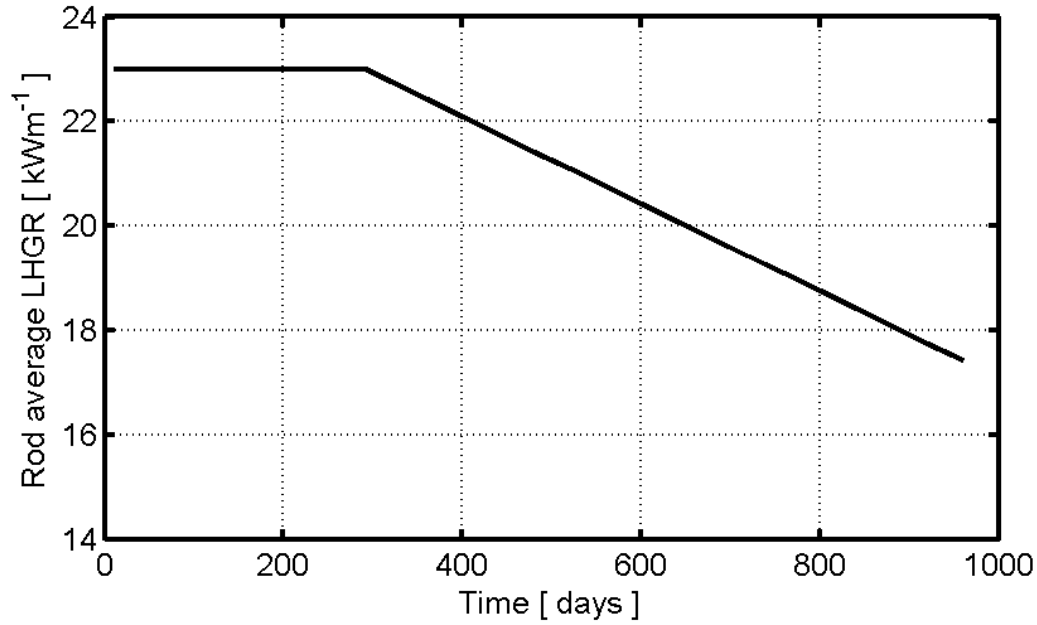

Figure 2.1: Steady-state irradiation history for the PWR fuel rod.

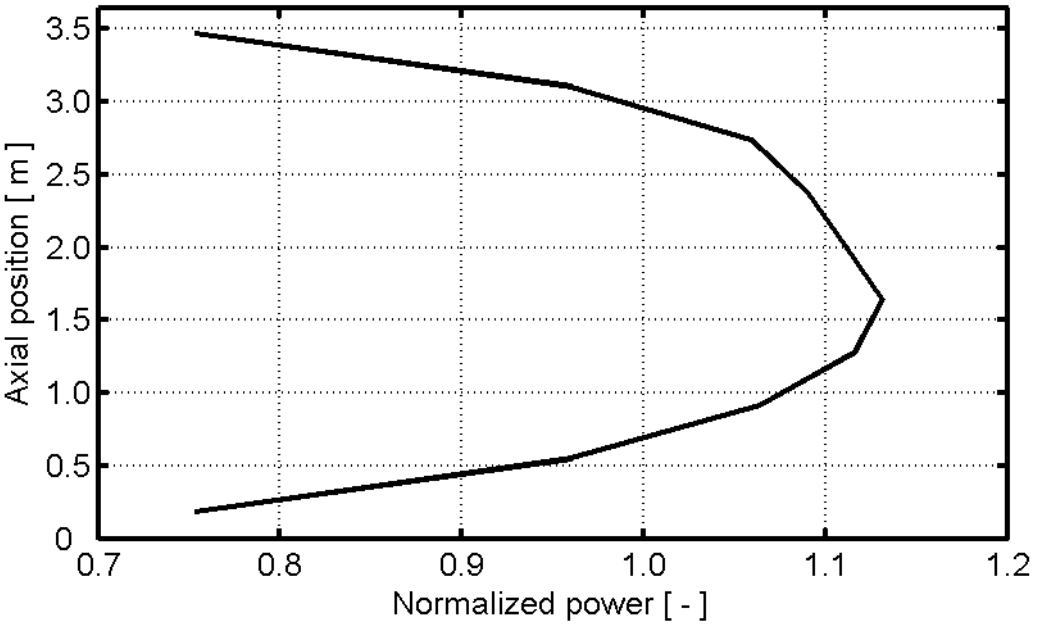

Figure 2.2: Axial power distribution for the PWR fuel rod. This power profile was used under both steady-state irradiation and subsequent RIA.

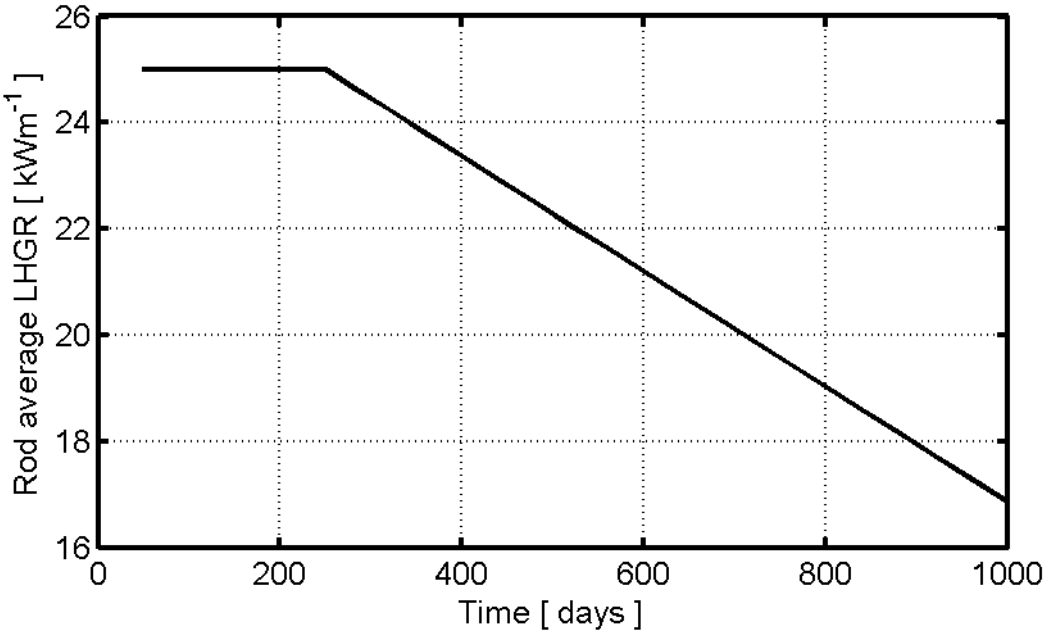

Figure 2.3: Steady-state irradiation history for the BWR fuel rod.

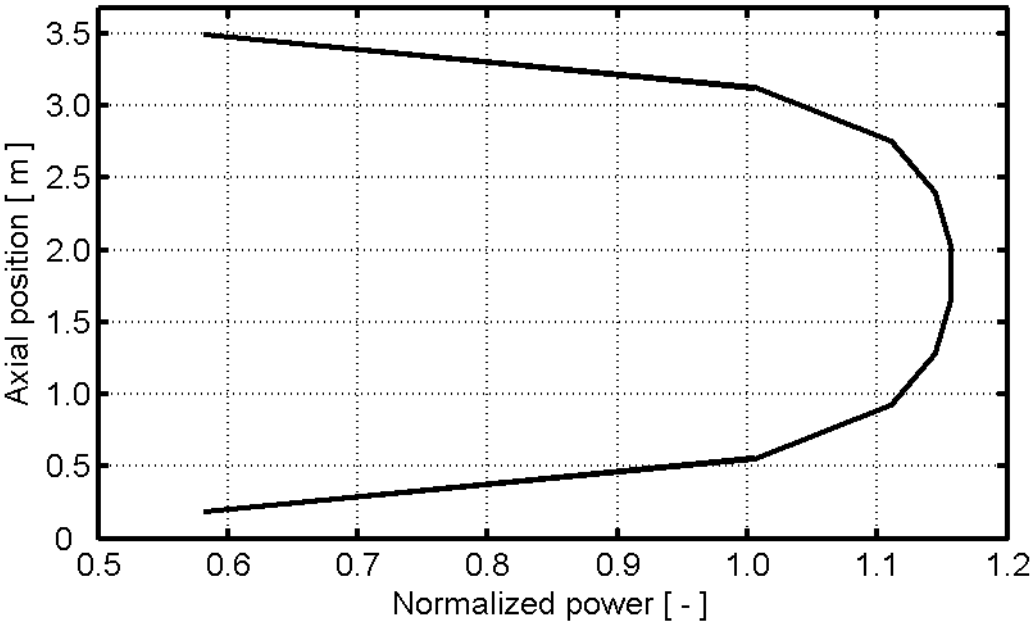

Figure 2.4: Axial power distribution for the BWR fuel rod. This power profile was used under both steady-state irradiation and subsequent RIA.

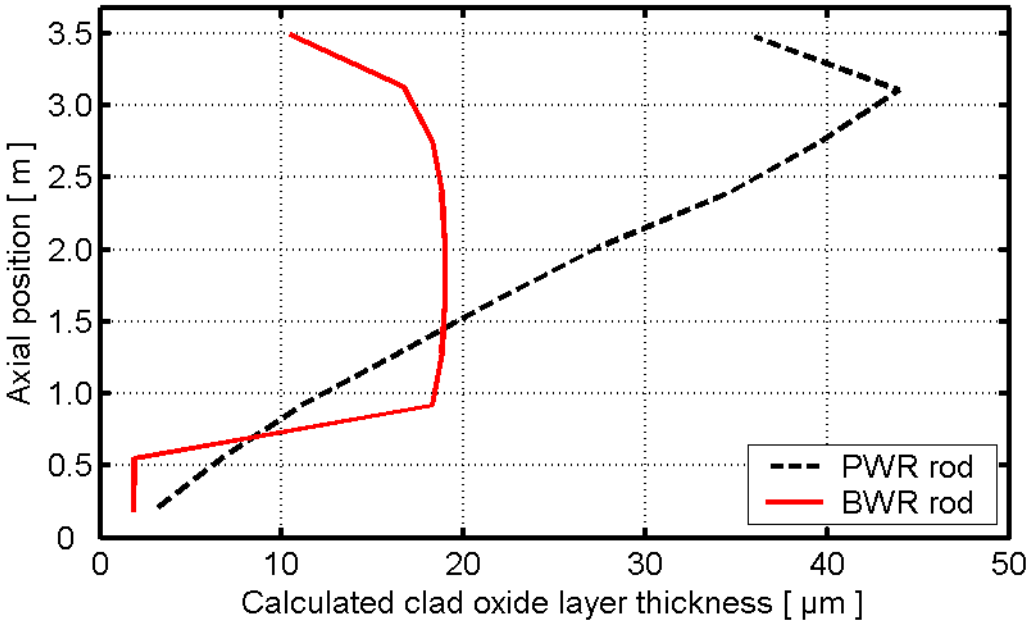

Figure 2.5: Calculated clad oxide layer thickness at end of base irradiation, i.e. at 42 MWd(kgU)$^{-1}$ rod average burnup, by use of best-estimate models in FRAPCON-3.2.

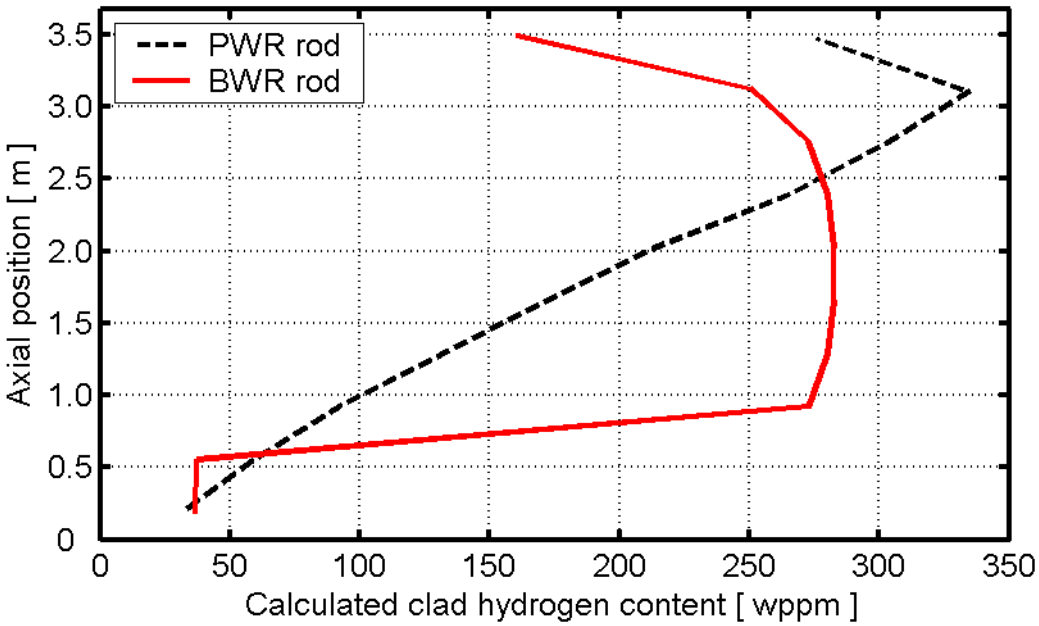

Figure 2.6: Calculated clad radial average hydrogen content at end of base irradiation, i.e. at 42 MWd(kgU)$^{-1}$ rod average burnup, by use of best-estimate models in FRAPCON-3.2.

2.3 Postulated reactivity initiated accidents

The thermo-mechanical analyses of postulated RIAs presented here closely follow the evaluations performed with SIMULATE-3K by Vattenfall and OKG. Hence, for the postulated rod ejection accidents in PWRs, we use the same core conditions as applied by Gabrielson (2004) in analyses of hot zero power (HZP) REA in Ringhals 3. For the postulated control rod drop accidents in BWRs, we use the same core conditions as applied by Wiksell (2003) in analyses of cold zero power (CZP) CRDA in Oskarshamn 3. The assumed core conditions are summarized in table 2.3.

All analyses were performed by use of the SCANAIR-3.2 computer code, in which the extended coolant channel model was applied; see section 5.1. The applied models for clad-to-water heat transfer are thus given in the right column of table 5.1. All analyses were restricted to the fuel burnup specified in section 2.2, i.e. to a rod average burnup of 42 MWd(kgU)$^{-1}$, which in this case corresponds to a radial average axial peak burnup of 48 MWd(kgU)$^{-1}$. The rod axial power distributions used in analyses of RIA were identical to those used in simulations of steady-state irradiation; see figures 2.2 and 2.4. Hence, for simplicity, a fixed axial power profile was assumed throughout the steady-state base irradiation and the subsequent reactivity initiated accident.[1]

The strain-based clad failure criterion proposed by Jernkvist et al. (2003) was used in analyses in order to determine the threshold conditions for fuel rod failure. In addition, this criterion was compared with the failure criterion proposed by Rashid et al. (2000) in the parametric study of pulse width; see section 4.

Parameter		**PWR HZP REA**	**BWR CZP CRDA**
Initial power	[% of nominal]	0.1	0.01
Coolant pressure	[MPa]	15.5	0.1
Coolant inlet temperature	[K]	564.9	303.1
Subchannel mass flow	[gs^{-1}]	327.5	61.1
Subchannel mass flux	[kg(m^{2}s)$^{-1}$]	3759	657.2

Table 2.3: Core conditions applied in simulations of reactivity initiated accidents.

[1] In the assessment of burnup-dependent fuel rod failure thresholds, reported by Jernkvist and Massih (2004), a different axial power profile was applied in transient analyses of the HZP REA.

3 Influence of power pulse shape

3.1 Definition of generic power pulse shapes

The core analyses performed with SIMULATE-3K yield a spectrum of power pulses, with large variations in pulse width and amplitude. Key properties of calculated pulses for PWR REA at HZP are summarized in table 3.1, whereas the results for BWR CRDA at CZP are given in table 3.2. The data in table 3.1 refer to local conditions in the peak power node, i.e. to the fuel assembly and axial node with maximum heat generation rate. The data in table 3.2 refer to local conditions in the peak power axial node of two specific fuel assemblies; D287 and E545 (Wiksell, 2003). In both tables, $\Delta\rho$ denotes the worth of the ejected/dropped control rod, β is the fraction of delayed neutrons, P_{max} is the maximum power in percent of nominal, t_{max} is the time at which the maximum power is attained, and τ is the full width at half maximum (FWHM) of the power pulse.

REA case	$\Delta\rho$ [10^{-5}]	β [10^{-5}]	P_{max} [%]	t_{max} [ms]	τ [ms]
R2-BLX-F06	764	502	18 042	125.2	30.5
R2-BLX-H02	759	502	17 054	131.8	28.7
R2-EOFP-F06	853	444	32 601	113.9	23.6
R2-EOFP-H02	856	444	31 973	114.0	23.1
R3-BLX-F06	824	517	22 323	126.3	25.3
R3-BLX-H02	823	517	19 838	129.0	26.8
R3-EOFP-F06	821	453	23 234	129.1	25.0
R3-EOFP-H02	816	453	22 155	130.3	25.9

Table 3.1: Summary of calculated power pulses in three-dimensional analyses of HZP REA in Ringhals 2 and 3 with SIMULATE-3K (Gabrielson, 2004).

CRDA case	$\Delta\rho$ [10^{-5}]	β [10^{-5}]	P_{max} [%]	t_{max} [ms]	τ [ms]
LCM-1300-D287 (normal drop)	1300	569	50 465	225.4	45.2
LCM-1300-D287 (fast drop)	1300	569	74 882	170.2	31.5
LCM-1500-D287 (normal drop)	1500	569	71 205	206.1	35.4
LCM-1500-D287 (fast drop)	1500	569	105 987	153.5	25.3
NH-800-E545	800	562	2 798	837.7	68.9
NH-1000-E545	1000	562	6 497	732.2	48.2
NH-1200-E545	1200	562	8 868	667.1	43.9
NH-1500-E545	1500	562	11 379	593.8	42.9

Table 3.2: Summary of calculated power pulses in three-dimensional analyses of CZP CRDA in Oskarshamn 3 with SIMULATE-3K (Wiksell, 2003).

In order to allow a comparison of pulse shapes, each calculated power pulse in tables 3.1 and 3.2 was first normalized by use of the following relations

$$P' = P / P_{max}, \tag{3.1}$$

$$t' = (t - t_{max}) / \tau. \tag{3.2}$$

The calculated PWR REA pulses are plotted in normalized form, $P'(t')$, in figure 3.1. The comparison in figure 3.1 reveals similarity in shape of the ascending flank of the normalized pulses, but the tails of the pulses differ. The most significant differences are found between the pulses at beginning (BLX) and end (EOFP) of the reactor operating cycle, whereas the core and fuel design, i.e. Ringhals 2 (R2) or Ringhals 3 (R3), seems to be of minor importance to the pulse shape.

The calculated BWR CRDA pulses are plotted in normalized form, $P'(t')$, in figure 3.2. Also in this case, the ascending flanks of the normalized pulses are similar, but the tails of the pulses differ. The CRDAs under nuclear heating (NH) show much more pronounced tails than the events under local criticality measurements (LCM).

In order to assess the impact of power pulse shape on the calculated fuel rod failure thresholds, we first defined six "generic" pulse shapes: three for PWR REA and three for BWR CRDA. These were derived by simply taking the arithmetic averages of selected subsets of the normalized pulses in figures 3.1 and 3.2. Each generic pulse shape was then used in determination of the fuel rod failure threshold, and calculated results obtained with different pulse shapes were finally compared.

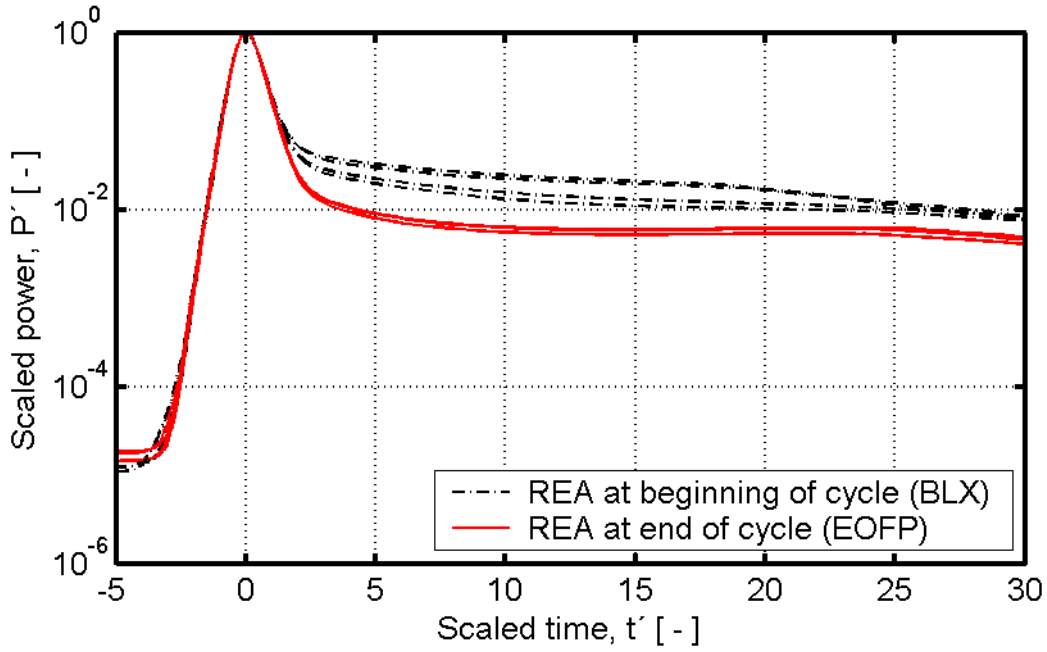

Figure 3.1: Normalized power pulse shapes for PWR REA. The eight calculated pulses defined in table 3.1 were normalized through eqs. (3.1) and (3.2).

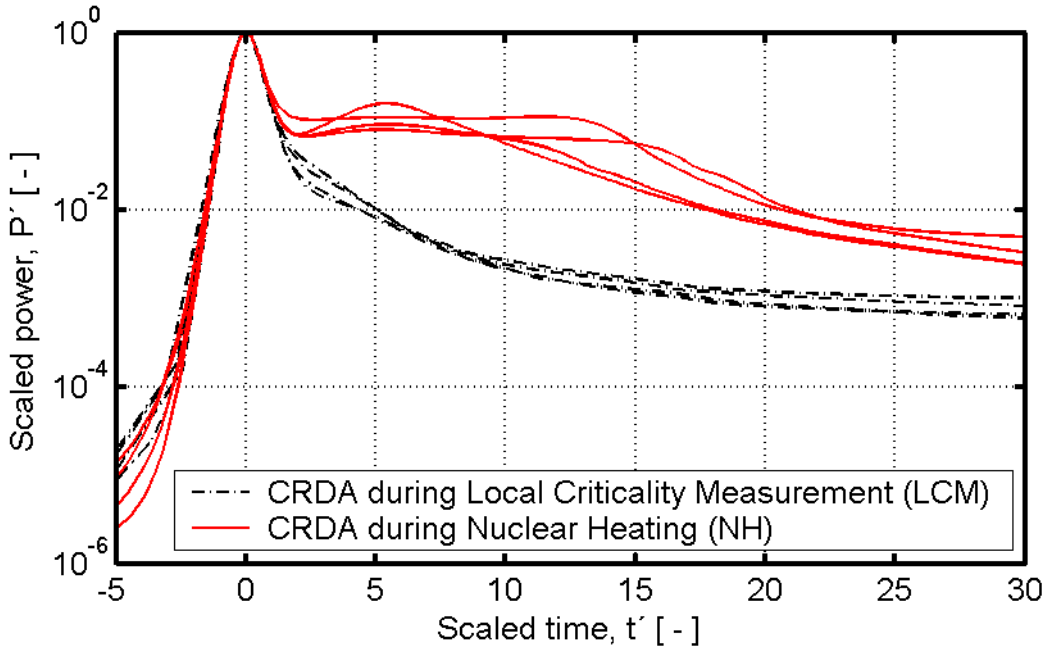

Figure 3.2: Normalized power pulse shapes for BWR CRDA. The eight calculated pulses defined in table 3.2 were normalized through eqs. (3.1) and (3.2).

In addition to the six generic pulse shapes derived from figures 3.1 and 3.2, we also used a simple Gaussian power pulse, defined by

$$P'(t') \quad = \quad P'_o + (1 - P'_o)\, e^{-2.7726(t')^2} \tag{3.3}$$

Here, P'_o is the normalized initial power level. The Gaussian function in eq. (3.3) is symmetric with respect to t'=0, which is obviously not the case for the calculated power pulses in figures 3.1 and 3.2.

The three generic power pulses used in analyses of PWR REA are shown in figure 3.3, together with the Gaussian pulse. The generic pulses correspond to:

- Arithmetic average of all 8 normalized pulses in figure/table 3.1 (BLX+EOFP)
- Arithmetic average of the 4 normalized pulses in figure/table 3.1, related to beginning of cycle conditions (BLX)
- Arithmetic average of the 4 normalized pulses in figure/table 3.1, related to end of cycle conditions (EOFP)

The three generic power pulses used in analyses of BWR CRDA are shown in figure 3.4, together with the Gaussian pulse. The generic pulses correspond to:

- Arithmetic average of all 8 normalized pulses in figure/table 3.2 (NH+LCM)
- Arithmetic average of the 4 normalized pulses in figure/table 3.2, related to nuclear heating conditions (NH)
- Arithmetic average of the 4 normalized pulses in figure/table 3.2, related to local criticality measurement conditions (LCM)

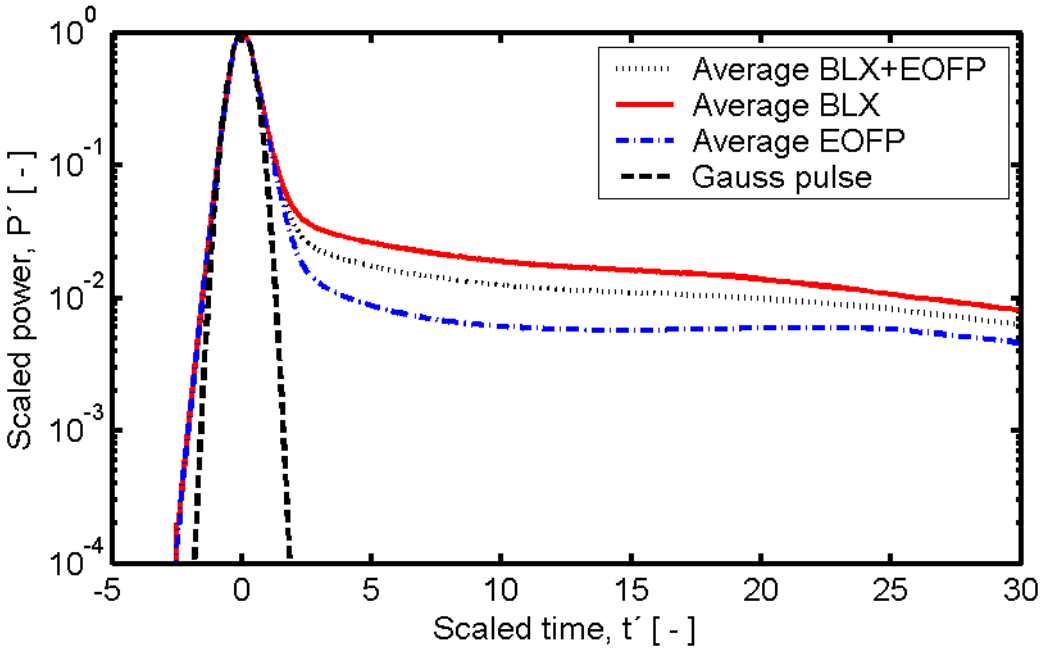

Figure 3.3: Power pulses (normalized) used in parametric study of PWR REA.

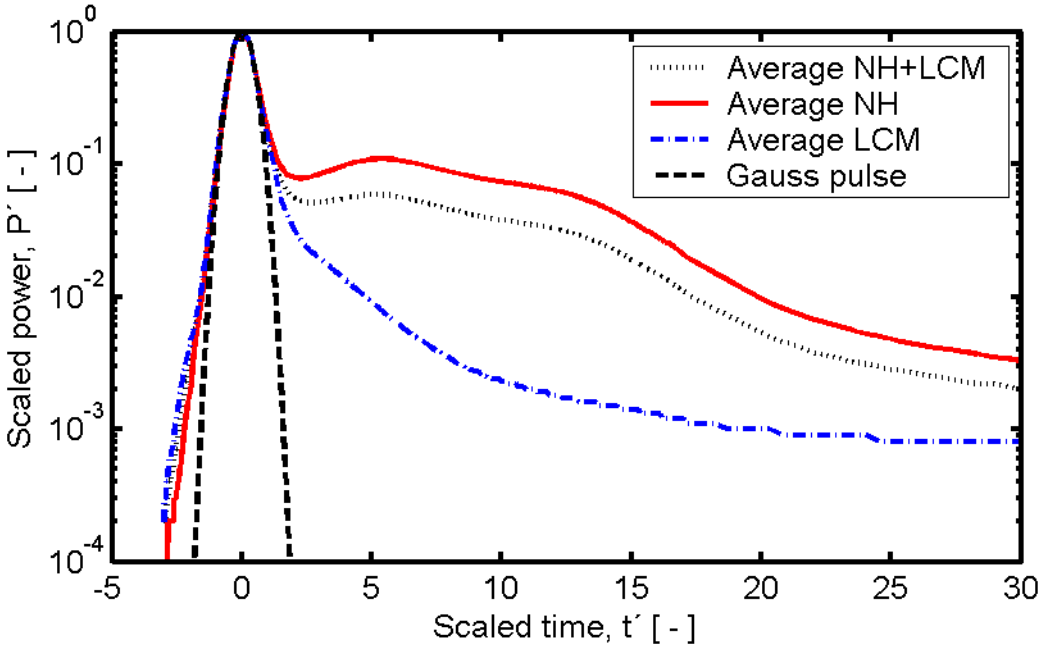

Figure 3.4: Power pulses (normalized) used in parametric study of BWR CRDA.

In the performed analyses, the pulse width τ was set to fixed values. Based on the calculated pulse widths in tables 3.1 and 3.2, τ was set to 25 ms in analyses of PWR REA and to 45 ms in analyses of BWR CRDA. These pulse widths are those used in determination of clad failure thresholds for RIA in PWRs and BWRs (Jernkvist & Massih, 2004). The time to maximum power, t_{max}, was set to 3τ in all analyses.

The pulse amplitude, P_{max}, was taken as a free parameter, and SCANAIR-3.2 was run in an iterative loop in order to determine the pulse amplitude at which clad failure was predicted. Once this threshold pulse amplitude was found, iterations were terminated and the corresponding threshold fuel enthalpy and other key fuel rod parameters were evaluated. This computational procedure was followed for each of the power pulses defined above, and the results are presented in the following subsections.

3.2 Results for PWR HZP REA

Table 3.3 summarizes calculated key fuel rod properties at threshold conditions, i.e. conditions obtained for a power pulse with just sufficient amplitude to induce clad tube failure under the considered PWR HZP REA. As shown by the first line of the table, this amplitude is somewhat (1.3%) higher for the Gaussian pulse than for the other pulse shapes. Although the critical pulse amplitudes are almost the same for all considered pulse shapes, the maximum fuel enthalpy differs between the pulses. These differences are due to the tails of the power pulses, shown in figure 3.3. The highest fuel enthalpy is obtained for the BLX pulse shape, which has the most pronounced tail. The impact of pulse shape is clearly seen in the evolution of fuel enthalpy with respect to time, which is plotted in figure 3.5 for the considered pulse shapes.

		Assumed pulse shape			
Parameter		**Average BLX+EOFP**	**Average BLX**	**Average EOFP**	**Gaussian pulse**
Max LHGR (rod average)	[MWm^{-1}]	10.96	10.96	10.96	11.10
Max fuel enthalpy	[$J(gUO_2)^{-1}$]	696	758	667	634
Max enthalpy increase	[$J(gUO_2)^{-1}$]	623	685	594	562
Max injected energy	[$J(gUO_2)^{-1}$]	920	1029	816	609
Time to max fuel enthalpy	[ms]	716	746	126	101
Max fuel temperature	[K]	2672	2838	2550	2497
Max clad temperature	[K]	1467	1521	1418	1330
Max clad hoop plastic strain	[%]	9.43	11.81	6.51	3.47
Time to DNB	[ms]	87.3	87.3	84.1	87.3
Time to clad failure	[ms]	92.5	92.5	92.5	92.5
Clad temperature at failure	[K]	977.3	977.4	977.2	984.1
Clad hoop plastic strain at failure	[%]	1.70	1.70	1.70	1.78
Axial position of clad failure	[m]	1.46-1.83	1.46-1.83	1.46-1.83	1.46-1.83

Table 3.3: Predicted impact of power pulse shape on the fuel rod failure behaviour under PWR HZP REA. The calculations were performed for a power pulse width of 25 ms and a rod average burnup of 42 $MWd(kgU)^{-1}$. Presented enthalpies and energies are axial peak radial average values.

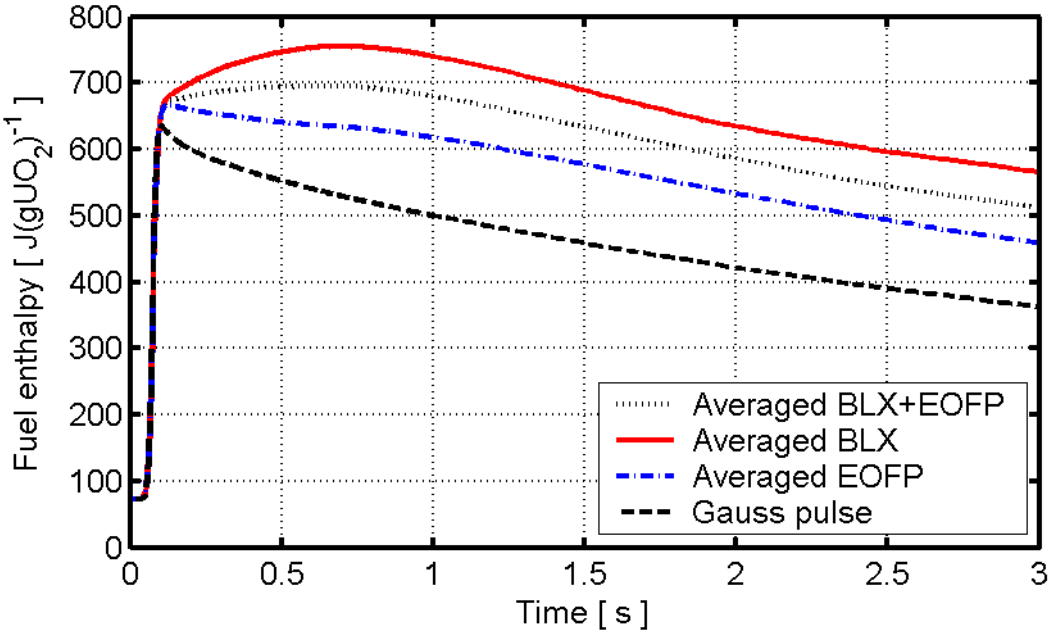

Figure 3.5: Calculated fuel radial average enthalpy with respect to time for the considered REA power pulses. The fuel enthalpy is evaluated at the axial node at which clad failure is predicted (1.46-1.83 m from bottom of the rod).

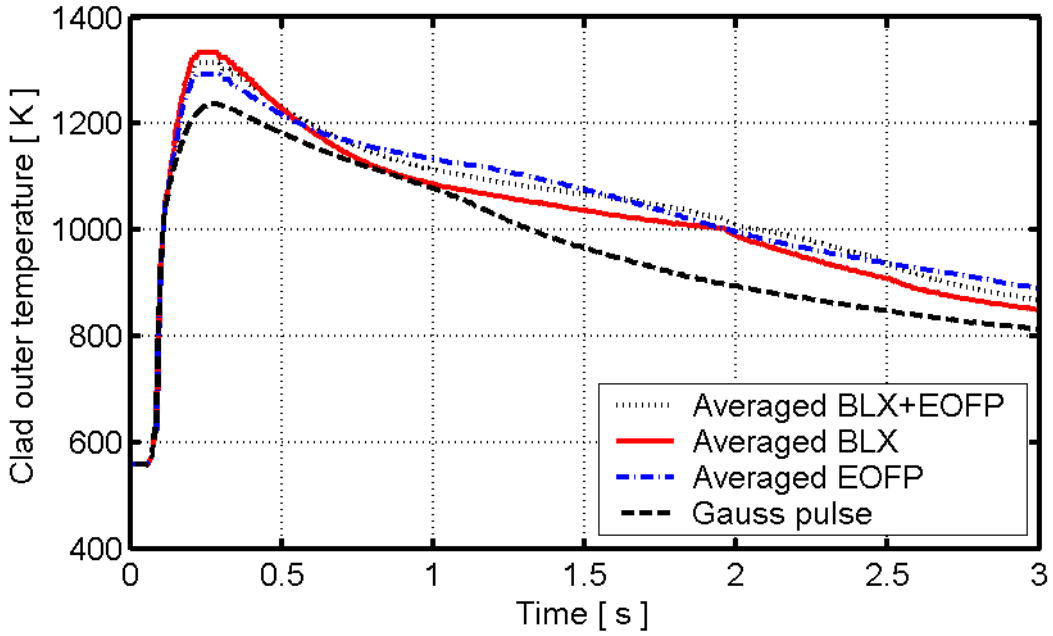

Figure 3.6: Calculated clad outer surface temperature with respect to time for the considered REA power pulses. The clad temperature is evaluated at the axial node at which clad failure is predicted (1.46-1.83 m from bottom of the fuel rod).

Moreover, it is interesting to note that the Gaussian pulse, which has no tail at all, yields the lowest maximum fuel enthalpy. Consequently, the application of a Gaussian pulse shape in calculations of fuel rod failure thresholds implies a conservative assumption. The conservatism is however moderate, since the calculated maximum enthalpy at failure is just 4.9 % lower for the Gaussian pulse than for the EOFP pulse shape, which is the most restricting of the pulses determined from three-dimensional core analyses with SIMULATE-3K. As shown in the upper half of table 3.3, the Gaussian pulse also yields the lowest maximum temperatures and deformations.

The calculated evolution of clad temperature is shown in figure 3.6 for the considered power pulses. At the axial position of clad failure, departure from nucleate boiling (DNB) is predicted at 84-87 ms, which is just before the cladding fails. After DNB, the clad temperature increases rapidly as a result of film boiling with very poor clad-to-water heat transfer.

The lower part of table 3.3 presents cladding properties, evaluated at the time and axial position at which clad failure takes place. The axial segment (node), in which the clad is predicted to fail, is identical for all considered pulse shapes. The failure node corresponds to the peak power axial position of the fuel rod, see figure 2.2, which means that this node is also the position at which the maximum fuel enthalpy is reached.

Clad failure is predicted early in the transient, and the calculated time to failure is 92.5 ms, irrespective of pulse shape. Since the considered pulses are very similar in shape up to this point in time, the clad temperature and hoop plastic strain at failure are similar for all the pulses.

3.3 Results for BWR CZP CRDA

Table 3.4 summarizes calculated key fuel rod properties at threshold conditions for the considered BWR CZP CRDA, evaluated with the four different pulse shapes shown in figure 3.4. The tails of these pulses differ considerably, and that is also clearly reflected in the calculated results in table 3.4:

Firstly, we note that the Gaussian power pulse yields the lowest enthalpies, temperatures and deformations. In particular, the calculated maximum fuel enthalpy (failure threshold) is 3.3 % lower for the Gaussian pulse than for the LCM pulse shape, which is the most restricting of the pulses determined from three-dimensional core analyses with SIMULATE-3K. This corroborates the conclusion drawn in section 3.2, that the use of a Gaussian power pulse leads to moderate conservatism in calculated fuel rod failure enthalpies.

Secondly, the cladding is predicted to fail under the early heat-up stage of the transient for the Gaussian- and LCM-pulses, but at a much later stage for the other two pulse shapes. Hence, the predicted failure mode is disparate for these two pulse categories, and the calculated clad hoop plastic strains at failure differ by almost an order of magnitude. To this end, it should be noticed that the failure criterion used in our analyses is applicable only to the low-strain failure mode obtained for the Gaussian- and LCM-pulse (Jernkvist et al., 2003).

Thirdly, the axial position at which the cladding is predicted to fail is dependent on the pulse shape. A comparison with figure 2.4 reveals that clad failure at the rod peak power axial position is foreseen only for the Gaussian power pulse. The fuel enthalpies and energies presented in table 3.4 are axial peak values, and thus represent the conditions at the failure position only for the Gaussian pulse. However, the calculated fuel enthalpy and clad outer surface temperature at the position of clad failure are plotted with respect to time in figures 3.7 and 3.8. The large differences in calculated clad temperature evolution between the four cases are due to the fact that the data pertain to different axial positions, with very different cooling conditions.

	Assumed pulse shape			
Parameter	**Average NH+LCM**	**Average NH**	**Average LCM**	**Gaussian pulse**
Max LHGR (rod average) [MWm^{-1}]	5.75	4.36	7.02	7.30
Max fuel enthalpy [$J(gUO_2)^{-1}$]	700	691	635	614
Max enthalpy increase [$J(gUO_2)^{-1}$]	698	689	633	612
Max injected energy [$J(gUO_2)^{-1}$]	927	923	788	672
Time to max fuel enthalpy [ms]	899	979	236	182
Max fuel temperature [K]	2571	2556	2431	2407
Max clad temperature [K]	1661	1645	1540	1538
Max clad hoop plastic strain [%]	12.46	11.41	5.70	3.55
Time to clad dry-out [ms]	188	208	198	170
Time to clad failure [ms]	3209	2109	216	164
Clad temperature at failure [K]	816	725	693	846
Clad hoop plastic strain at failure [%]	11.8	9.51	1.49	1.60
Axial position of clad failure [m]	2.21-2.58	1.10-1.47	0.37-0.74	1.84-2.21

Table 3.4: Predicted impact of power pulse shape on the fuel rod failure behaviour under BWR CZP CRDA. The calculations were performed for a power pulse width of 45 ms and a rod average burnup of 42 $MWd(kgU)^{-1}$. Presented enthalpies and energies are axial peak radial average values.

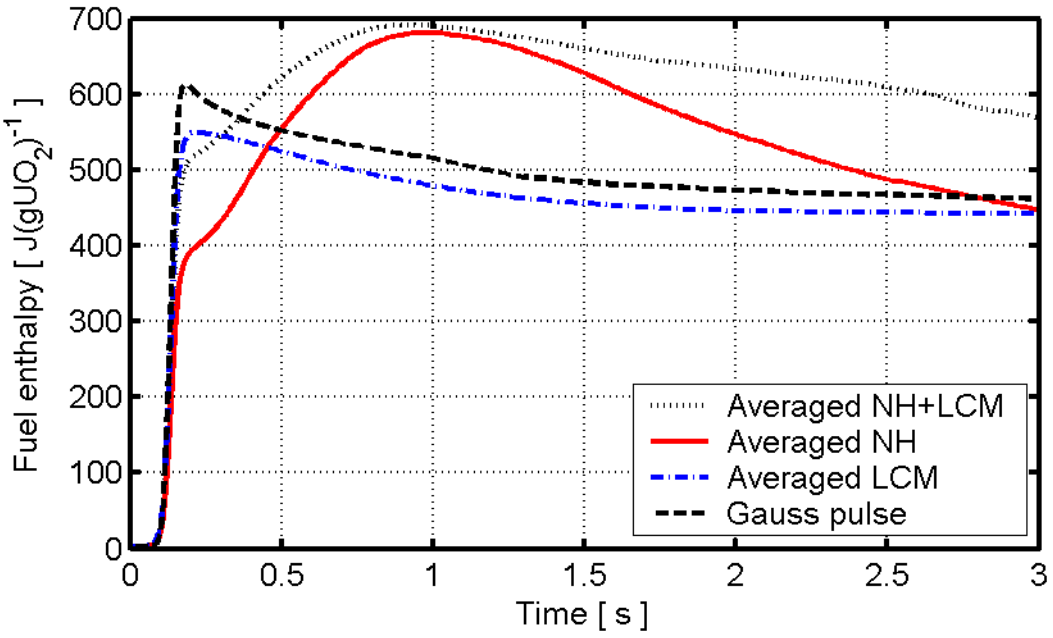

Figure 3.7: Calculated fuel radial average enthalpy with respect to time for the considered CRDA power pulses. For each pulse, the fuel enthalpy is evaluated at the axial position at which clad failure is predicted; see table 3.4.

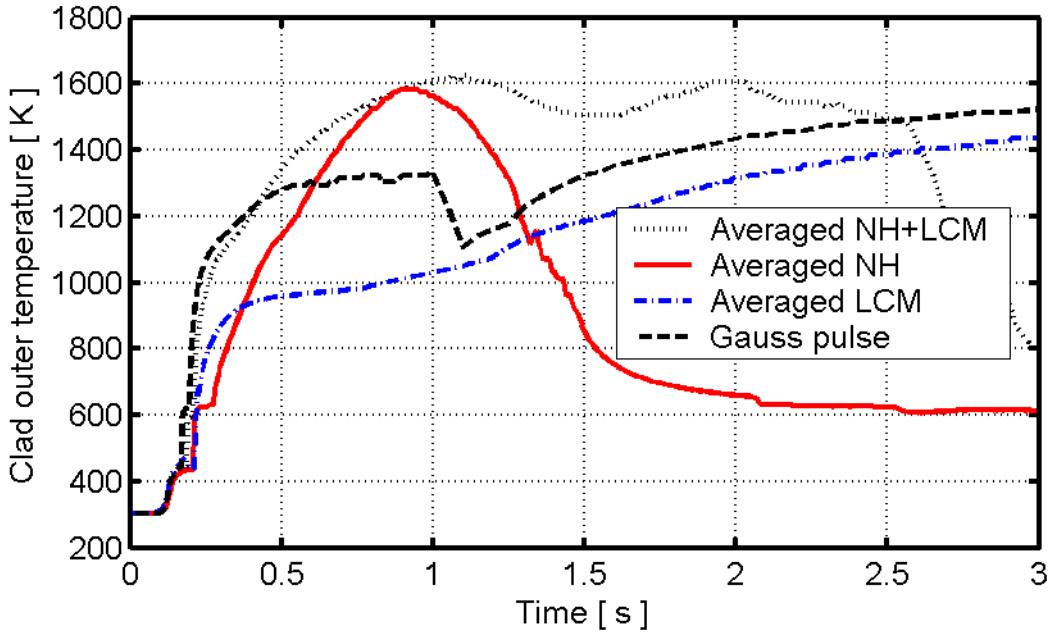

Figure 3.8: Calculated clad outer surface temperature with respect to time for the considered CRDA power pulses. For each pulse, the clad temperature is evaluated at the axial position at which clad failure is predicted; see table 3.4.

4 Influence of power pulse width

The impact of pulse width on the fuel rod failure behaviour was studied by calculating the fuel rod failure thresholds for PWR and BWR fuel, using different pulse widths. More precisely, a Gaussian pulse shape was used in the calculations, and the pulse was given six different pulse widths in the range from 5 to 100 ms. In addition, a 50 s long quasi-stationary power pulse was included in the study for comparison.

For each of the pulse widths, the fuel enthalpy threshold for failure and other key fuel properties were evaluated by an iterative search for the pulse amplitude, at which the cladding was predicted to fail. All analyses were performed for a rod average burnup of 42 MWd(kgU)$^{-1}$. Hence, the computational procedure followed the same pattern as in the preceding section.

4.1 Results for PWR HZP REA

Table 4.1 summarizes key fuel rod parameters at threshold conditions, i.e. conditions obtained for a power pulse with just sufficient amplitude to induce clad tube failure under the considered PWR HZP REA. Evidently, the fuel rod failure threshold in terms of allowable fuel enthalpy depends strongly on the pulse width. This is illustrated in figure 4.1, which shows the calculated maximum fuel enthalpy and enthalpy increase, plotted with respect to pulse width. In particular for pulses shorter than approximately 50 ms, the pulse width seems to have a strong impact on the fuel rod failure threshold.

From table 4.1, it is clear that clad failure is predicted before DNB for power pulses shorter than 25 ms, whereas the opposite is true for longer pulses. This has significance to the clad temperature at failure, which is fairly high for the longer pulses. Moreover, the higher temperature also implies a larger clad ductility, which results in increasing plastic strain at failure for pulses longer than 10 ms, as shown in figure 4.2.

The calculated maximum clad strain energy density is presented in table 4.1. The strain energy density has been proposed by the Electric Power Research Institute (EPRI) as a clad ductility parameter, claimed to be appropriate for use in clad failure criteria (Rashid et al., 2000). For comparison, we present in table 4.1 a damage index D_{EPRI}, which is calculated from the failure criterion proposed by EPRI through

$$D_{EPRI} = \frac{SED}{CSED} . \tag{4.1}$$

Here, *SED* is the strain energy density calculated by SCANAIR-3.2, and *CSED* is the critical strain energy density, calculated through the correlation proposed by Rashid et al. (2000). Hence, $D_{EPRI} \geq 1$ implies clad failure, whereas $D_{EPRI} < 1$ means survival. Obviously, the EPRI failure criterion predicts survival for all cases considered here, which indicates that it is less restrictive than the criterion used in our analyses. This is in line with earlier comparisons of the two criteria, but the very low values presented for D_{EPRI} in table 4.1 may be misleading.

As discussed by Jernkvist et al. (2003), the calculation of D_{EPRI} in eq. (4.1) can possibly be biased by the fact that the stress-strain relation used for calculation of SED in SCANAIR-3.2 is different from the one used by Rashid et al. (2000) for evaluations of CSED from mechanical property tests.

4.2 Results for BWR CZP CRDA

Table 4.2 summarizes key fuel rod parameters at threshold conditions, i.e. conditions obtained for a power pulse with just sufficient amplitude to induce clad tube failure under the considered BWR CZP CRDA. The calculated fuel rod failure threshold in terms of allowable fuel enthalpy is plotted with respect to pulse width in figure 4.3. Just as for the PWR REAs analysed in the preceding section, the pulse width seems to have a significant impact on the fuel rod failure threshold for pulses shorter than approximately 50 ms.

From the calculated results in table 4.2, it is clear that clad failure is predicted before clad dry-out for pulses shorter than 100 ms. The calculated clad temperatures at failure are consequently low. In comparison with the PWR HZP REAs analysed in the preceding section, the calculated clad temperatures at failure are lower under BWR CZP CRDA. This is due to the differences in initial clad and coolant temperature between these postulated events; see table 2.3.

Figure 4.4 shows the calculated hoop plastic strain at failure. The failure strains are smaller than for the PWR HZP REAs analysed in the preceding section, as a consequence of lower clad temperatures. Moreover, there is an apparent decrease in failure strain for pulses wider than 50 ms, which results from the change in axial position of clad failure for the 100 ms wide pulse; see table 4.2. Hence, the axial position of clad failure seems to be affected not only by the shape of the power pulse, as found in section 3.3, but also by the pulse width.

Parameter	Pulse width (FWHM) 5 ms	10 ms	25 ms	30 ms	50 ms	100 ms	50 s
Max rod average LHGR [MWm^{-1}]	39.79	22.16	11.10	9.58	6.41	3.50	0.070
Max fuel enthalpy [$J(gUO_2)^{-1}$]	493	534	634	651	703	739	846
Max enthalpy increase [$J(gUO_2)^{-1}$]	420	461	561	578	630	666	773
Max injected energy [$J(gUO_2)^{-1}$]	437	486	609	631	703	768	7663
Time to max fuel enthalpy [ms]	21	41	101	123	202	402	172200
Max fuel temperature [K]	2284	2330	2497	2526	2604	2636	3222
Max clad temperature [K]	1155	1196	1330	1354	1431	1500	1119
Max clad hoop plastic strain [%]	1.07	1.54	3.47	3.90	5.43	7.74	4.14
Max clad hoop strain rate [s^{-1}]	2.78	1.57	0.89	0.90	0.90	0.78	0.006
Max clad strain energy density [MPa]	9.9	10.4	14.2	14.5	15.2	14.5	18.1
Time to DNB [ms]	29	45	87	105	162	302	No DNB
Time to clad failure [ms]	19	35	92	108	183	376	149000
Clad temperature at failure [K]	724	769	984	994	1147	1335	695
Clad hoop plastic strain at failure [%]	0.83	0.86	1.78	1.76	2.81	4.35	2.07
Axial position of clad failure [m]	1.46-1.83	1.46-1.83	1.46-1.83	1.46-1.83	1.46-1.83	1.46-1.83	0.73-1.10
Max clad damage index, D_{EPRI} [-]	0.32	0.34	0.46	0.47	0.51	0.48	0.60

Table 4.1: Predicted impact of power pulse width on the fuel rod failure behaviour under PWR HZP REA. The calculations were made for a rod average burnup of 42 $MWd(kgU)^{-1}$, using a power pulse with Gaussian shape.

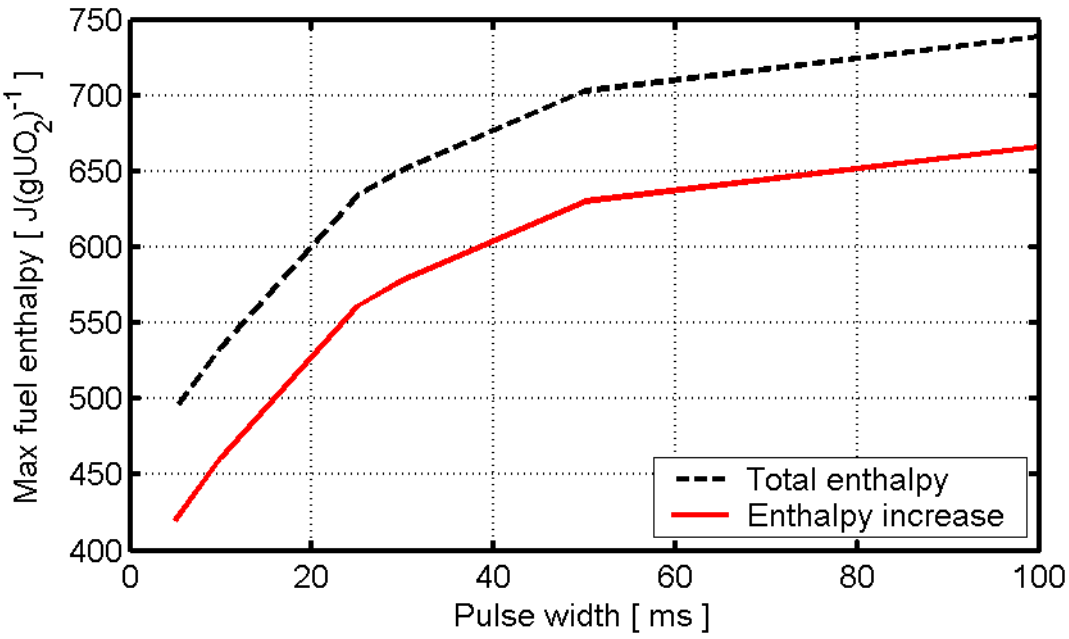

Figure 4.1: Calculated fuel rod failure threshold for PWR HZP REA in terms of allowable fuel radial average enthalpy for various pulse widths. The calculations were made for a rod average burnup of 42 MWd(kgU)$^{-1}$, using a Gaussian power pulse.

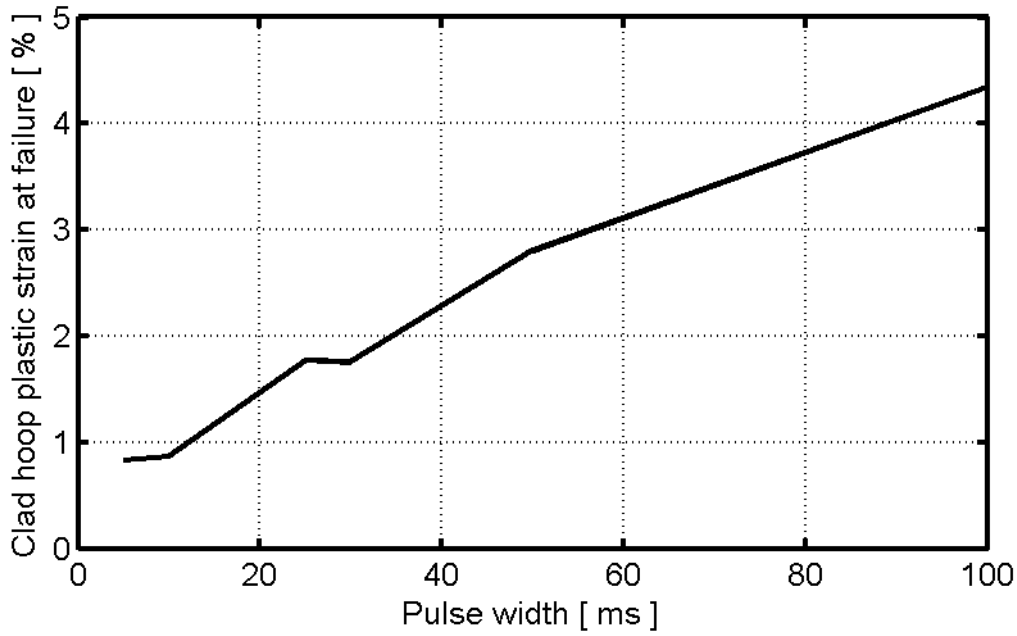

Figure 4.2: Calculated clad hoop plastic strain at failure vs. pulse width for PWR HZP REA. The strain is evaluated at the axial position and time at which the clad tube is predicted to fail.

Parameter	Pulse width (FWHM) 5 ms	10 ms	30 ms	45 ms	50 ms	100 ms	50 s
Max rod average LHGR [MWm^{-1}]	42.87	24.25	10.31	7.30	6.70	3.47	0.055
Max fuel enthalpy [$J(gUO_2)^{-1}$]	428	477	588	614	624	623	656
Max enthalpy increase [$J(gUO_2)^{-1}$]	425	474	586	612	621	620	654
Max injected energy [$J(gUO_2)^{-1}$]	439	497	634	672	686	711	5671
Time to max fuel enthalpy [ms]	21	42	123	182	202	401	159500
Max fuel temperature [K]	2136	2201	2382	2407	2418	2367	2869
Max clad temperature [K]	1234	1360	1364	1562	1560	1511	1407
Max clad hoop plastic strain [%]	0.67	1.00	2.78	3.55	3.88	4.06	7.85
Max clad hoop strain rate [s^{-1}]	2.75	1.58	0.69	0.52	0.51	0.30	0.01
Max clad strain energy density [MPa]	11.9	12.9	18.7	19.8	20.4	19.4	17.6
Time to clad dry-out [ms]	61	70	136	170	185	409	131000
Time to clad failure [ms]	18	40	111	164	182	410	185250
Clad temperature at failure [K]	449	618	794	846	858	634	550
Clad hoop plastic strain at failure [%]	0.58	0.86	1.39	1.60	1.69	1.40	1.39
Axial position of clad failure [m]	1.84-2.21	1.84-2.21	1.84-2.21	1.84-2.21	1.84-2.21	0.37-0.74	1.84-2.21
Max clad damage index, D_{EPRI} [-]	0.79	0.54	0.56	0.60	0.62	0.59	0.53

Table 4.2: Predicted impact of power pulse width on the fuel rod failure behaviour under BWR CZP CRDA. The calculations were made for a rod average burnup of 42 $MWd(kgU)^{-1}$, using a power pulse with Gaussian shape.

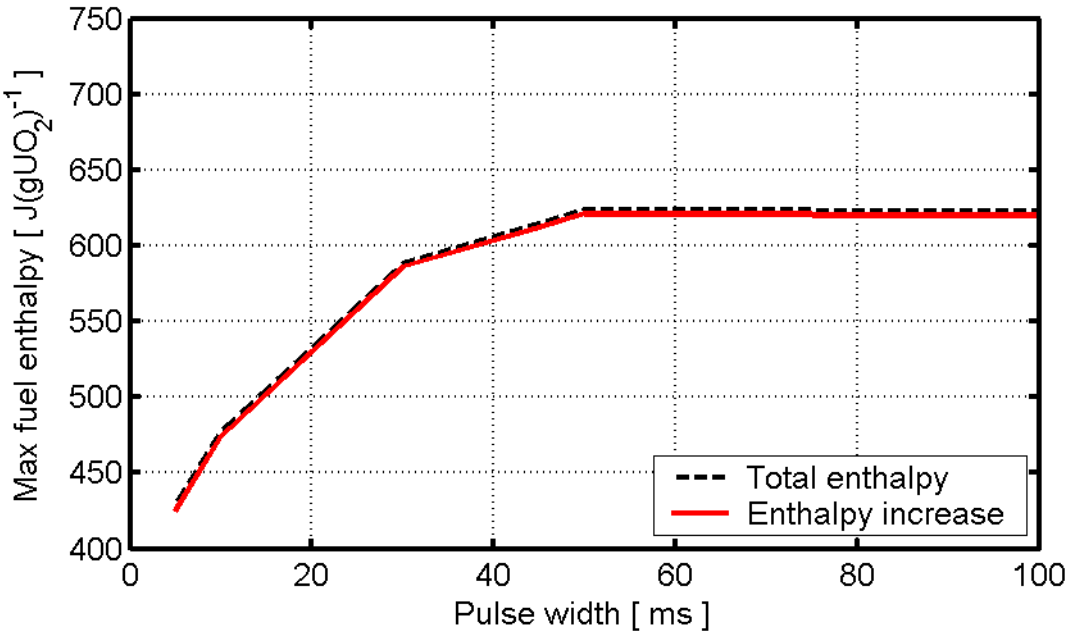

Figure 4.3: Calculated fuel rod failure threshold for BWR CZP CRDA in terms of allowable fuel radial average enthalpy for various pulse widths. The calculations were made for a rod average burnup of 42 MWd(kgU)$^{-1}$, using a Gaussian power pulse.

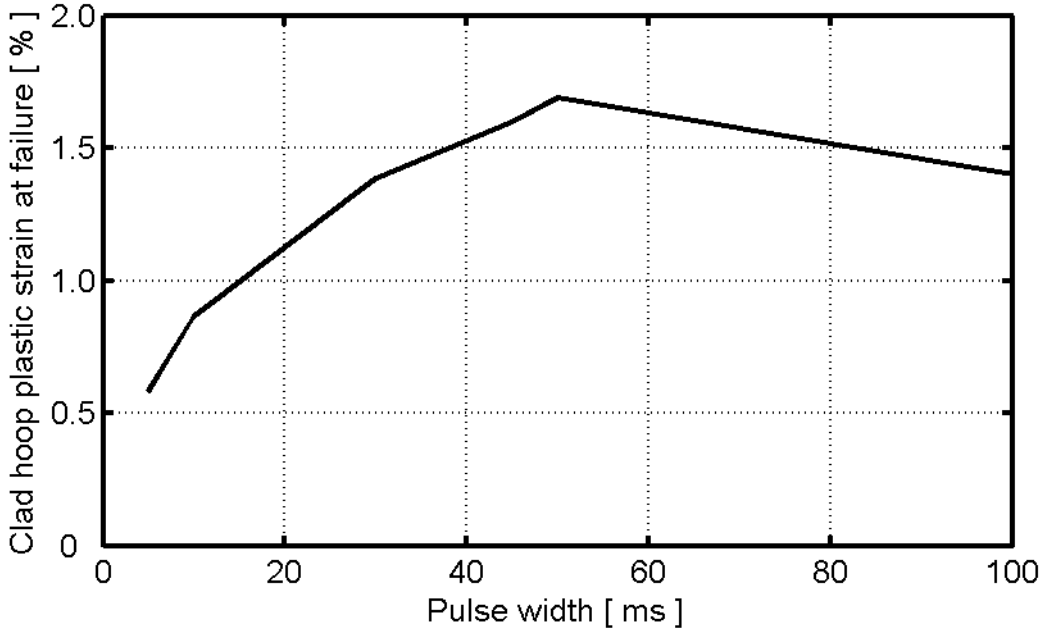

Figure 4.4: Calculated clad hoop plastic strain at failure vs. pulse width for BWR CZP CRDA. The strain is evaluated at the axial position and time at which the clad tube is predicted to fail.

5 Influence of clad-to-water heat transfer

As part of our assessment of fuel rod failure thresholds, SCANAIR-3.2 was extended with a new coolant channel model, allowing for two-phase flow and thus for simulations of BWR operating conditions. In the new model, the two-phase water coolant is treated as a homogeneous mixture of liquid and steam in thermodynamic equilibrium, and the code is equipped with an extended set of clad-to-water heat transfer correlations, which is applicable to both PWR and BWR conditions. In table 5.1, the new set of correlations is compared with the standard models in SCANAIR-3.2. Most of the correlations in table 5.1 are described in a review of heat transfer correlations for light water reactor application, recently published by the IAEA (2001).

Heat transfer regime	Standard SCANAIR-3.2	Extended SCANAIR-3.2
Forced convection to liquid phase	Dittus-Boelter	Dittus-Boelter
Subcooled nucleate boiling	Thom	Thom
Saturated nucleate boiling	-	Chen
Film boiling	Bishop-Sandberg-Tong	Groeneveld
Transition boiling	-	Condie-Bengtson
Forced convection to vapour phase	-	Dittus-Boelter
Critical heat flux	Babcock & Wilcox	EPRI-Columbia

Table 5.1: Clad-to-water heat transfer correlations used in SCANAIR-3.2.

5.1 Correlations for heat transfer under film boiling

The impact of supercritical clad-to-water heat transfer on the fuel rod failure threshold was studied by comparing three different correlations for clad-to-water heat transfer under film boiling. The correlations are documented in appendix A, and their claimed ranges of application are summarized in table 5.2. It is clear that the film boiling correlation by Groeneveld has the widest range of application, although the data presented in table 5.2 are not definite; other ranges for the correlations can be found in literature.

Correlation (reference)	Steam quality [-]	Pressure [MPa]	Mass flux [$kg(m^2s)^{-1}$]
Bishop-Sandberg-Tong (1965)	0.07 - 1.00	4.1 – 22	700 - 3140
Groeneveld (1973)	-0.12 - 3.09	0.07 – 22	130 - 4000
Dougall-Rohsenow (1963)	< 0.50	< 3.50	1660 - 3650

Table 5.2: Approximate ranges of application for the film boiling heat transfer correlations under study. Data from a review published by the IAEA (2001).

5.2 Results for PWR HZP REA

An REA at hot zero power was simulated, using a Gaussian power pulse. As in the analyses of pulse shapes in section 3.2, the pulse width was set to 25 ms. The pulse amplitude was also set to a fixed value, corresponding to the fuel rod failure threshold. Calculations were performed for four different sets of clad-to-water heat transfer models in SCANAIR-3.2:

1. The original models, as defined in table 5.1.
2. The extended coolant channel model, as defined in table 5.1. This set of correlations is used in determination of the burnup-dependent fuel rod failure threshold (Jernkvist & Massih, 2004).
3. The extended coolant channel model, but with the Groeneveld model substituted with the Dougall-Rohsenow film boiling correlation.
4. The extended coolant channel model, with film boiling (FB) completely suppressed. This was accomplished by postulating a very high critical heat flux.

Calculated key fuel properties are presented in table 5.3 for each of these four cases. Except for the cladding temperature and critical heat flux, differences between the cases are hardly found. The maximum fuel enthalpy is obviously not affected by the clad-to-water heat transfer models, and the same is true for the fuel rod failure behaviour. The damage index, D_{QT}, presented in table 5.3 is defined as the ratio of calculated clad hoop plastic strain, $\varepsilon_{\theta\theta}^{p}$, to the failure strain, ε_f,

$$D_{QT} = \frac{\varepsilon_{\theta\theta}^{p}}{\varepsilon_f} . \tag{5.1}$$

Here, $D_{QT} \geq 1$ implies clad failure, whereas $D_{QT} < 1$ means survival (Jernkvist et al., 2003). Evidently, the applied clad-to-water heat transfer models have a hardly noticeable effect on the calculated damage index. Hence, the calculated fuel rod failure threshold is not affected significantly by these models.

The calculated maximum clad-to-water heat fluxes in table 5.3 should be compared with the typical value of 6 MWm^{-2}, which has recently been reported from the PATRICIA transient heat transfer experiments under PWR cooling conditions by Bessiron (2004). The maximum heat flux calculated with the extended coolant channel model and the Groeneveld film boiling correlation (case 2 in table 5.3) is close to this value.

The evolution of clad temperature depends on the models for water-to-coolant heat transfer, as shown in figure 5.1. The film boiling correlation by Dougall and Rohsenow yields a much higher clad-to-water heat transfer coefficient than the correlations by Groeneveld and Bishop-Sandberg-Tong under PWR cooling conditions, and the calculated clad temperature is therefore lower for this model; see appendix A for details.

Parameter		Coolant-to-water heat transfer models (1) Original	(2) Extended	(3) Extended	(4) No FB
Max LHGR (rod average)	[MWm^{-1}]	11.10	11.10	11.10	11.10
Max fuel enthalpy	[$J(gUO_2)^{-1}$]	637	634	634	634
Max enthalpy increase	[$J(gUO_2)^{-1}$]	561	561	561	561
Max injected energy	[$J(gUO_2)^{-1}$]	609	609	609	609
Time to max fuel enthalpy	[ms]	101	101	101	101
Max fuel temperature	[K]	2503	2497	2497	2497
Max clad temperature	[K]	1424	1330	1179	1171
Max clad hoop plastic strain	[%]	3.54	3.47	3.14	3.04
Max clad-to-water heat flux	[MWm^{-2}]	3.09	6.28	8.11	13.55
Max clad damage index, D_{QT}	[-]	0.98	1.00	1.00	1.00
Time to clad failure	[ms]	92.5	92.5	92.5	92.5
Clad temperature at failure	[K]	1012	984	984	980
Clad hoop plastic strain at failure	[%]	1.81	1.78	1.78	1.77
Axial position of clad failure	[m]	1.46-1.83	1.46-1.83	1.46-1.83	1.46-1.83

Table 5.3: Predicted impact of clad-to-water heat transfer models on the fuel rod failure behaviour under PWR HZP REA. The calculations were performed for a 25 ms wide Gaussian power pulse and a rod average burnup of 42 MWd(kgU)$^{-1}$. Presented enthalpies and energies are axial peak radial average values.

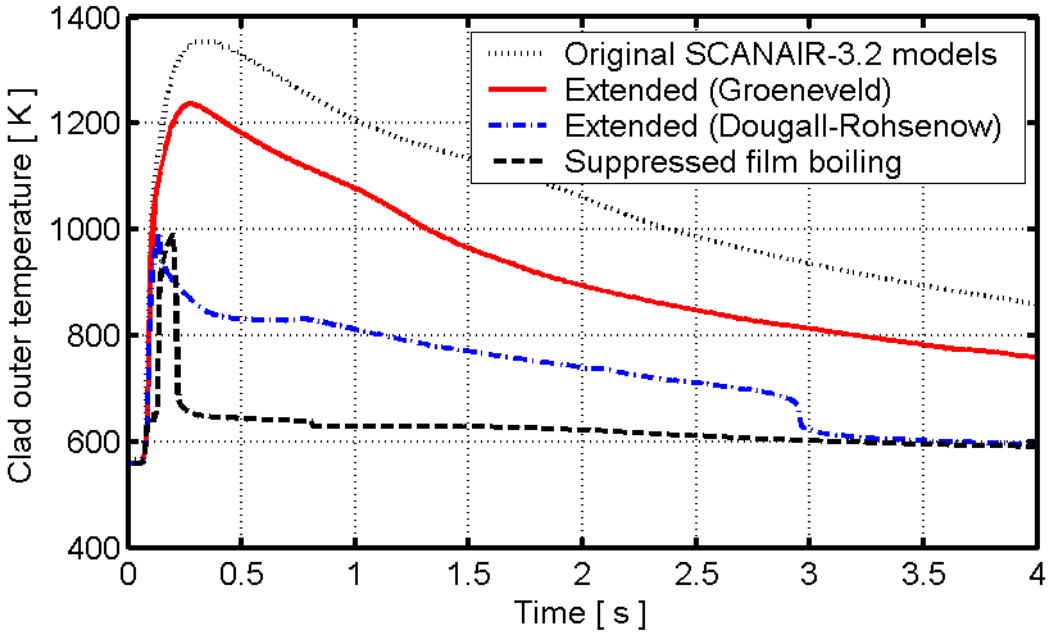

Figure 5.1: Evolution of clad outer surface temperature under HZP REA, calculated with four different sets of clad-to-water heat transfer correlations. The clad temperatures are evaluated at the predicted axial position of clad failure (1.46-1.83 m from bottom of the fuel rod).

5.3 Results for BWR CZP CRDA

A CRDA at cold zero power was simulated, using a Gaussian power pulse. As in the analyses of pulse shapes in section 3.3, the pulse width was set to 45 ms. The pulse amplitude was also set to a fixed value, corresponding to the fuel rod failure threshold. Calculations were performed for three different sets of clad-to-water heat transfer models in SCANAIR-3.2:

1. The extended coolant channel model, as defined in table 5.1.
2. The extended coolant channel model, but with the Groeneveld model substituted with the Dougall-Rohsenow film boiling correlation.
3. The extended coolant channel model, with film boiling completely suppressed. This was accomplished by postulating a very high critical heat flux.

Calculated key fuel properties are presented in table 5.4 for each of these three cases. In general, the differences are small. A striking exception is the maximum clad temperature, which is very much higher when calculated with the Dougall-Rohsenow film boiling correlation than with the other sets of models. This is further explored in figure 5.2, which shows the calculated evolution of clad surface temperature. From the expressions given for the Dougall-Rohsenow correlation in appendix A, it is evident that this model yields a very low (≈10 $W(m^2K)^{-1}$) clad-to-water heat transfer coefficient when both the steam quality and the pressure are low. For this reason, the model is not appropriate for application to atmospheric pressures.

Parameter		(1) Extended	(2) Extended	(3) No FB
Max LHGR (rod average)	[MWm^{-1}]	7.30	7.30	7.30
Max fuel enthalpy	[$J(gUO_2)^{-1}$]	614	614	614
Max enthalpy increase	[$J(gUO_2)^{-1}$]	612	612	611
Max injected energy	[$J(gUO_2)^{-1}$]	672	672	672
Time to max fuel enthalpy	[ms]	182	182	185
Max fuel temperature	[K]	2407	2407	2406
Max clad temperature	[K]	1562	1822	1361
Max clad hoop plastic strain	[%]	3.55	3.38	3.55
Max clad-to-water heat flux	[MWm^{-2}]	13.25	13.18	14.92
Max clad damage index, D_{QT}	[-]	1.00	1.00	1.03
Time to clad failure	[ms]	164	164	169
Clad temperature at failure	[K]	846	846	866
Clad hoop plastic strain at failure	[%]	1.60	1.60	1.78
Axial position of clad failure	[m]	1.84-2.21	1.84-2.21	1.84-2.21

Table 5.4: Predicted impact of clad-to-water heat transfer models on the fuel rod failure behaviour under BWR CZP CRDA. The calculations were performed for a 45 ms wide Gaussian power pulse and a rod average burnup of 42 $MWd(kgU)^{-1}$. Presented enthalpies and energies are axial peak radial average values.

The calculated maximum clad-to-water heat fluxes in table 5.4 are not too far from the typical value of 12 MWm^{-2}, which has recently been reported by Bessiron (2004) from PATRICIA transient heat transfer experiments performed under cooling conditions that were representative of the Japanese Nuclear Safety Research Reactor (NSSR). These cooling conditions involve stagnant water at ambient temperature (293 K) and atmospheric pressure, which is quite close to the cooling conditions used in our calculations; see table 2.3.

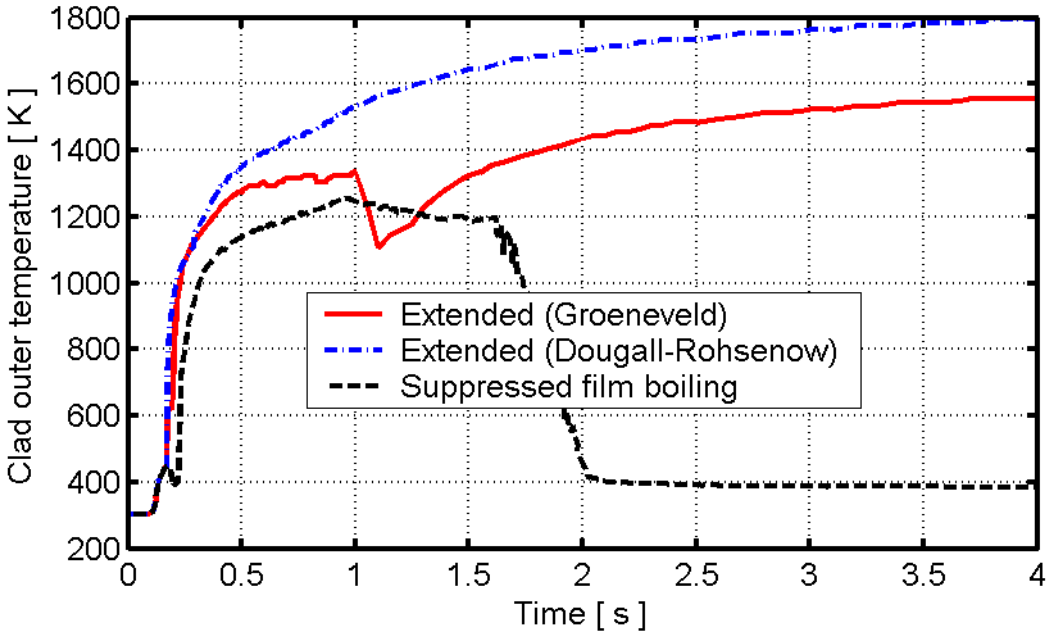

Figure 5.2: Evolution of clad outer surface temperature under CZP CRDA, calculated with three different sets of clad-to-water heat transfer correlations. The clad temperatures are evaluated at the predicted axial position of clad failure (1.84-2.21 m from bottom of the fuel rod).

6 Conclusions

In the presented parametric sensitivity study, we investigated the influence of applied pulse shape, pulse width and clad-to-water heat transfer models on the calculated fuel rod failure thresholds for reactivity initiated accidents. The results of our study indicate, that of the three factors investigated, only the pulse shape and pulse width have an impact on the calculated fuel rod failure thresholds, which are here defined in terms of maximum allowable radial average fuel enthalpy.

Although the models for clad-to-water heat transfer are important for accurate prediction of the clad temperature evolution during an RIA, the prediction of clad failure is in our study nearly unaffected by these models. The explanation to this rather surprising result is that clad failure is predicted early during the transient. At this early stage of an RIA, the clad temperature is governed primarily by the pellet-to-clad heat transfer and only to a lesser extent influenced by the clad-to-water heat transfer. It should be noticed that that this behaviour may be affected by transient spallation of the clad oxide layer, a supposedly important phenomenon, which was not addressed in our study (Bessiron, 2004).

The shape of the applied power pulse was found to have a significant impact on the calculated enthalpy threshold for fuel rod failure, both for PWR and BWR RIA. Our study was based on eight power pulses for PWR HZP REA and eight pulses for BWR CZP CRDA, all of which were obtained from three-dimensional core analyses of postulated RIAs with zero or near-zero initial power. The ascending flanks of these pulses were found to be similar in shape, whereas the tails of the pulses differed significantly. As a consequence, it is not possible to define a generic and realistic pulse shape to be applied in determination of the fuel rod failure threshold. To avoid the use of multiple pulse shapes in analyses, it is suggested that a simple Gaussian pulse is applied for this purpose. As shown in our study, the use of a Gaussian power pulse leads to moderate conservatism in the calculated failure threshold. More precisely, the threshold enthalpies calculated with a Gaussian power pulse are about 5% lower than those calculated with the most restricting of the realistic pulse shapes obtained from three-dimensional core analyses (EOFP-pulses for PWR and LCM-pulses for BWR).

Also the width of the applied power pulse was found to affect the calculated enthalpy threshold for fuel rod failure, in particular for power pulses shorter than about 50 ms. For both the PWR HZP REA and the BWR CZP CRDA considered in our study, the enthalpy threshold was found to drop by approximately 200 $J(gUO_2)^{-1}$ when reducing the pulse width from 50 to 5 ms. Based on these results, we conclude that the pulse width is an important parameter in calculations of fuel rod failure thresholds for RIA.

Evaluation of power pulses from the performed three-dimensional core analyses indicates that lower-end pulse widths are approximately 25 ms for REA at HZP, and 45 ms for CRDA at CZP.

These pulse widths are in line with those reported in literature by Diamond et al. (2002) and Stelletta and Waeckel (1997). Pulse widths of 25 and 45 ms will therefore be used in the determination of failure thresholds for PWR and BWR fuel rods, respectively. Our parametric study shows that a change in postulated pulse width from 25 to 20 ms would lower the calculated fuel enthalpy threshold for PWR fuel by approximately 30 $J(gUO_2)^{-1}$. Likewise, a change in postulated pulse width from 45 to 40 ms would lower the calculated fuel enthalpy threshold for BWR fuel by 10 $J(gUO_2)^{-1}$. These numbers follow from our analysis of a fuel rod with 42 $MWd(kgU)^{-1}$ rod average burnup, and do not necessarily apply to other burnups.

Finally, the performed parametric study indicates that the axial position of clad failure is dictated by several interacting factors, such as the axial distributions of power, clad oxide and hydrogen content. The predicted position of clad failure was also found to be affected by the variation in coolant properties along the fuel rod, which to a certain extent controls the clad temperature distribution. Moreover, the axial position of failure was also influenced by the shape and width of the applied power pulse.

7 References

Berna, G.A., Beyer, C.E., Davis, K.L. and Lanning, D.D., 1997.
FRAPCON-3: A Computer Code for the Calculation of Steady-State, Thermal-Mechanical Behavior of Oxide Fuel Rods for High Burnup,
NUREG Report NUREG/CR-6534, Volume 2 (1997).

Bessiron, V., 2004.
Clad-to-Coolant Heat Transfer during a RIA Transient: Analysis of the PATRICIA Experiments, Modelling and Applications, Paper presented at the Fuel Safety Research Meeting, Tokyo, Japan, March 1-2 2004.

Bishop, A.A., Sandberg, R.O. and Tong, L.S., 1965.
Forced Convection Heat Transfer at High Pressures after the Critical Heat Flux,
ASME Paper 65-HT-31.

Diamond, D.J., Bromley, B.P. and Aronson, A.L., 2002.
Pulse Width in a Rod Ejection Accident, Proc. of the NEA CSNI Topical Meeting on RIA Fuel Safety Criteria, Aix-en-Provence, France, May 13-15 2002.

Dougall, R.S. and Rohsenow, W.M., 1963.
Film-Boiling on the Inside of Vertical Tubes with Upward Flow of the Fluid at Low Qualities, Heat Transfer Lab Report MIT-9079-26, Department of Mechanical Engineering, Massachusetts Institute of Technology, Cambridge, USA.

Federici, E., Lamare, F., Bessiron, V. and Papin, J., 2000.
Status of Development of the SCANAIR Code for the Description of Fuel Behavior under Reactivity Initiated Accidents, Proc. of the 2000 Int. Topical Meeting on LWR Fuel Performance, Park City, Utah, USA, April 10-13 2000.

Gabrielson, P., 2004.
Effektpulskaraktäristik vid RIA för PWR, (In Swedish)
Vattenfall Bränsle Report PB-236/03, January 2004.

Groeneveld, D.C., 1973.
Post-Dryout Heat Transfer at Reactor Operating Conditions,
AECL Report AECL-4513.

IAEA, 2001.
Thermohydraulic Relationships for Advanced Water Cooled Reactors,
Report IAEA-TECDOC-1203, International Atomic Energy Agency, Vienna, Austria.

Jernkvist, L.O. and Massih, A.R., 2004.
Assessment of Fuel Rod Failure Thresholds under Reactivity Initiated Accidents,
Quantum Technologies Report TR 04-009, Uppsala, Sweden.

Jernkvist, L.O., Massih, A.R. and Rudling, P., 2003.
A Strain-Based Clad Failure Criterion for Reactivity Initiated Accidents in Light Water Reactors, Quantum Technologies Report TR 03-008, Uppsala, Sweden.

Rashid, Y.R., Montgomery, R.O., Lyon, W.F. and Yang, R., 2000.
A Cladding Failure Model for Fuel Rods Subjected to Operational and Accident Transients, Proc. of the IAEA Technical Committee Meeting on Nuclear Fuel Behaviour Modelling at High Burnup and its Experimental Support, Windermere, UK, June 19-23 2000.

Stelletta, S. and Waeckel, N., 1997.
Fuel Failure Risk Assessment under Rod Ejection Accident in PWR's Using the RIA Simulation Tests Database – the French Utility Position,
Proc. of the 1997 Int. Topical Meeting on LWR Fuel Performance, Portland, Oregon, USA, March 2-6 1997, pp 721-728.

Wiksell, G., 2003.
Pulsbredder vid transienter beräknade med S3K, (In Swedish)
OKG Report 2003-08073.

Appendix A: Correlations for clad-to-water heat transfer under film boiling

The correlations for clad-to-water heat transfer under film boiling, which were studied in section 5 of the report, are documented in the sequel. The equations correspond exactly to the way the correlations are implemented in SCANAIR-3.2. It should be noticed that other fuel performance codes may have slightly different implementations of the same models.

All the film boiling correlations presented here are intended for application to dispersed two-phase flow (mist flow), where the liquid phase is distributed as droplets entrained in a continuous vapour phase. The correlations are based on the assumption of thermodynamic equilibrium between the two phases, which means that the coolant temperature is assumed to be at the equilibrium saturation temperature. However, in SCANAIR-3.2, the correlations are applied also to film boiling under subcooled conditions (inversed annular flow regime).

For all correlations, the clad-to-water heat flux, j ,is assumed to obey

$$j = h\left(T_w - T_c\right), \tag{A.1}$$

where h is the clad-to-water heat transfer correlation, T_w is the clad outer surface (oxide surface) temperature, and T_c is the coolant bulk temperature. As mentioned above, saturated water conditions are assumed when evaluating the heat transfer coefficient. The correlations thus yield an equivalent heat transfer coefficient, h_s, which satisfies

$$j = h_s\left(T_w - T_s\right), \tag{A.2}$$

where T_s is the water saturation temperature. In case of subcooled conditions ($T_c<T_s$), the clad-to-water heat transfer coefficient is obtained by equating the heat fluxes in eq. (A1) and eq. (A2), hence

$$h = h_s \frac{\left(T_w - T_s\right)}{\left(T_w - T_c\right)}. \tag{A.3}$$

A.1 Groeneveld

The correlation by Groeneveld (1973) is implemented in SCANAIR-3.2 through

$$h_s = 0.052 \frac{k_{vs}}{D_{hy}} \mathrm{Pr}_{vw}^{1.26} \mathrm{Re}_{vs}^{0.688} \gamma^{-1.06}. \tag{A.4}$$

Here, k_{vs} is the thermal conductivity of vapour at saturated water conditions and D_{hy} is the hydraulic diameter of the flow channel.

The Prandtl number for the vapour phase

$$\mathrm{Pr}_{vw} = \frac{C_{pv}(T_w)\,\mu_v(T_w)}{k_v(T_w)}, \tag{A.5}$$

is evaluated at the clad wall temperature, T_w, which is indicated in eqs. (A.4) and (A.5) by the subscript w. In eq. (A.5), C_{pv} denotes the heat capacity, k_v the thermal conductivity, and μ_v the dynamic viscosity of the vapour phase. The Reynolds number for two-phase flow

$$\mathrm{Re}_{vs} = \frac{G\,D_{hy}}{\mu_{vs}}\left(X_e + (1-X_e)\frac{\rho_{vs}}{\rho_{ls}} \right) \tag{A.6}$$

is evaluated at saturated vapour conditions. Here, G is the coolant mass flux, X_e is the equilibrium steam quality and ρ_{vs} and ρ_{ls} are the vapour and liquid densities at saturated conditions. Finally, the Miropolsky factor, γ, in eq. (A.4) is calculated through

$$\gamma = Max\left(0.1,\ 1-0.1\left(1-X_e\right)^{0.4}\left(\frac{\rho_{ls}}{\rho_{vs}}-1\right)^{0.4} \right). \tag{A.7}$$

A.2 Dougall-Rohsenow

The correlation by Dougall and Rohsenow (1963) is basically the well-known model for single-phase forced convection by Dittus and Boelter, which has been extended to mixed-phase flow by a modification to the Reynolds number, which is defined by eq. (A.6). The correlation is implemented in SCANAIR-3.2 through

$$h_s = 0.023\,\frac{k_{vs}}{D_{hy}}\,\mathrm{Pr}_{vs}^{0.4}\,\mathrm{Re}_{vs}^{0.8}\ . \tag{A.8}$$

Here, the Prandtl number for the vapour phase

$$\mathrm{Pr}_{vs} = \frac{C_{pv}(T_s)\,\mu_v(T_s)}{k_v(T_s)}, \tag{A.9}$$

is evaluated at the coolant saturation temperature, T_s, which is indicated in eq. (A.9) by the subscript s. The Reynolds number of the vapour phase is also evaluated at the saturation temperature, as given by eq. (A.6).

A.3 Bishop-Sandberg-Tong

The correlation by Bishop, Sandberg and Tong (1965) is the film boiling heat transfer model used in the original coolant channel model of SCANAIR-3.2. It is implemented through

$$h_s = 0.0193 \frac{k_{vf}}{D_{hy}} \mathrm{Pr}_{vf}^{1.23} \left(\frac{G D_{hy}}{\mu_{vf}} \right)^{0.8} \left(\frac{\rho_{vs}}{\rho_{ls}} \right)^{0.068} \beta^{0.68} . \quad \text{(A.10)}$$

Here, k_{vf} and μ_{vf} are the vapour phase thermal conductivity and dynamic viscosity at the vapour film temperature, which is taken as the arithmetic average of the clad outer surface temperature and the coolant bulk temperature

$$T_f = \frac{T_w + T_c}{2} . \quad \text{(A.11)}$$

Also the vapour phase Prandtl number in eq. (A.10) is evaluated at the film temperature, as indicated by the superscript *f*. Finally, the factor β in eq. (A.10) is given by

$$\beta = \left(X_e + (1 - X_e) \frac{\rho_{vs}}{\rho_{ls}} \right) . \quad \text{(A.12)}$$

A comment should be made to eq. (A.12):
As the original coolant channel model in SCANAIR-3.2 is restricted to single-phase liquid water, the equilibrium steam quality X_e is not calculated within the model. Instead, X_e is taken as an input parameter, which is applied to all axial positions of the fuel rod. Moreover, X_e is not allowed to change with time during the transient. In the analyses presented in section 5.2 of the report, X_e was set to 0. This corresponds to a coolant, consisting of liquid water at saturated conditions.

www.ski.se

STATENS KÄRNKRAFTINSPEKTION
Swedish Nuclear Power Inspectorate

POST/POSTAL ADDRESS SE-106 58 Stockholm
BESÖK/OFFICE Klarabergsviadukten 90
TELEFON/TELEPHONE +46 (0)8 698 84 00
TELEFAX +46 (0)8 661 90 86
E-POST/E-MAIL ski@ski.se
WEBBPLATS/WEB SITE www.ski.se